Journal of Materials Science: Materials in Electronics (2019) 30:6583–6592
https://doi.org/10.1007/s10854-019-00965-2

Inspired cheese-like biomass-derived carbon with plentiful heteroatoms for high performance energy storage

Yongchao Liu[1] · Minjie Shi[1] · Chao Yan[1] · Qiqi Zhuo[1] · Hanzhao Wu[1] · Lei Wang[1] · Hu Liu[2,3] · Zhanhu Guo[2]

Received: 3 November 2018 / Accepted: 18 February 2019 / Published online: 23 February 2019

Abstract
Directional construction of high performance carbon electrode from biomass plays a critical role in the development of energy storage devices. Herein, a straightforward and scalable route is reported to develop a cheese-like biomass-derived carbon electrode with plentiful heteroatoms for sodium-ion batteries and lithium-ion batteries by using egg white as a precursor. The resultant cheese-like structure provides more ion transport channels, shorter ion transport distance and increased charge transfer efficiency. At the same time, the self-doping by heteroatoms could offer high electronic conductivity and rich active sites. Benefited from the reasonable arrangement, the as-prepared electrode exhibits significantly enhanced sodium storage properties including highly reversible capacity (226.8 mA h g^{-1} at 100 mA g^{-1}), superior rate capability and excellent capacity retention (92.8%). It also shows great lithium ion capacity (567.5 mA h g^{-1} after 80 cycles at 100 mA g^{-1}), fine rate capability and outstanding capacity retention (104.8%). This work could shed light on the effective and scalable preparation of biomass-derived carbon for efficient energy storage applications.

1 Introduction

It's well known that Lithium-ion batteries (LIBs) are an important energy storage system, due to the relatively suitable output voltage, high energy density, low self-discharge, long cycle life and environment friendly [1, 2]. Compared to the limited resources of lithium in the earth, sodium-ion batteries (SIBs) have great advantage in energy storage, because of similar electrochemical storage behavior and more abundant of sodium resources [3, 4]. Carbon-based materials, especially commercial graphite, are still the dominant electrode material for application in LIBs because of their superior chemical stability, high electrical conductive and environment friendly [5]. However, the low charge storage theoretically capacity (372 mA h g^{-1}) of commercial graphite does not meet the requirements for high energy and high-power devices [6]. What's more, the larger radius of sodium ion than that of lithium ion, the slower ion diffusion and a small amount of embedded ions, lead to the capacity of sodium ion battery lower than that of lithium ion battery. Therefore, numerous smart strategies of promising carbon materials which have unique structures, fast ion and electron transmission channels and high specific surface area are explored for applications in SIBs and LIBs, such as carbon nanotubes (CNTs) [7], carbon nanofibers (CNFs) [8], carbon nanospheres [9] and graphene [10–12]. Nevertheless, the difficulty in adapting to large scale industrial production and relatively high cost limit their applications. Consequently, a method for facile and low cost production of carbon materials with excellent electrochemical properties remains much needed for energy storage applications.

Biomass-derived carbon materials have attracted much attention due to their low cost, wide distribution, green and renewable characteristics [13–15]. Accordingly, numerous biomasses (such as kiwifruit [16], peanut shell [17, 18], litchi shell [19], rice popcorn [20], bamboo carbon [21], wheat straw [22] and so on [23]) have been used as precursors to synthesize carbon materials. Nevertheless, those processes need to be carried out by activators or multi-steps

✉ Chao Yan
chaoyan@just.edu.cn

[1] School of Materials Science and Engineering, Jiangsu University of Science and Technology, Zhenjiang 212003, People's Republic of China

[2] Integrated Composites Laboratory (ICL), Department of Chemical & Biomolecular Engineering, University of Tennessee, Knoxville, TN 37996, USA

[3] Key Laboratory of Materials Processing and Mold (Zhengzhou University), Ministry of Education; National Engineering Research Center for Advanced Polymer Processing Technology, Zhengzhou University, Zhengzhou 450002, People's Republic of China

high temperature carbonization. Therefore, it is necessary to find a simple, efficient and green method to prepare high performance energy storage materials.

Herein, we report a one-step carbonization to synthesize biomass-derived carbon electrodes for SIBs and LIBs by using chicken egg white as a precursor. The obtained carbon materials exhibit cheese-like structure with plentiful heteroatoms. The cheese-like structure can provide more ion transport channels, shorter ion transport distance and increased charge transfer efficiency. At the same time, the self-doping by heteroatoms could offer high electronic conductivity and rich active sites. Attributed to the unique structure, the as-prepared electrodes present significantly enhanced sodium and lithium storage properties. It is expected that the present work could serve as an effective and scalable method to prepare biomass-derived carbon for efficient energy storage applications.

2 Experimental

2.1 Material preparation

Egg white was prepared by using egg white separator to remove yolk. Firstly, the egg white was strongly stirred into foam with a constant speed agitator. Then the foam was dried for 48 h in the freeze dryer. Subsequently, the egg white derived carbon was prepared by carbonizing the foam at 500, 600, 700 and 800 °C for 30 min under nitrogen atmosphere at a heating rate of 10 °C min^{-1}. After naturally cooling down to room temperature, the obtained carbon powder was grinded and washed with 80 °C deionize water and room temperature ethanol to remove occurring impurities, then the product was dried in vacuum at 80 °C for 24 h. According to the different carbonation temperature, these samples were denoted as EWPC-T (T = 500, 600, 700 and 800).

2.2 Material characterization

The surface morphology and particle sizes were analyzed with a JSM-6480 scanning electron microscope (SEM), and energy dispersive spectrometer (EDS) analysis was performed. X-ray photoelectron spectroscopy (XPS) using an ESCALAB 250Xi X-ray photoelectron spectrometer with Al–Kα X-rays as the excitation source was used to analyze the electronic structure. The phase structure of the samples was determined by using an X-ray diffraction (XRD-6000) with Cu Kα radiation (β = 0.15406 nm) operated at 40 KV and 30 mA at the 2θ range of 10°–80°. Raman spectra were carried out by using a micro-Raman spectrometer (Invia renishaw) in the back-scattering geometry with a 532 nm laser as the excitation source at room temperature. FTIR spectra (Nicolet 380) were used to identify the surface functional groups of these samples. Thermal gravimetric analysis (TGA) was performed on a Pyris Diamond TG-DTA by heating the freeze-dried egg white to 800 °C at a rate of 10 °C min^{-1} in nitrogen atmosphere.

2.3 Electrochemical measurements

The electrochemical tests were conducted by CR2025 coin-type half cells, which were assembled in an argon-filled glove box (H_2O, $O_2 < 0.1$ ppm). To prepare the testing electrode, a slurry with 80% active material, 10% carbon black (Super-p, TIMICAL) and 10% polyvinylidene fluoride (PVDF, HSV900) in suitable *N*-methyl pyrrolidine (NMP, AR) was coated onto a copper foil (10 μm) current collector (~ 1.5 mg of active material on each electrode) and then dried at 80 °C overnight in vacuum oven. Sodium metal and glass fiber were used as counter electrodes and separators in SIBs tests, respectively. The electrolyte was composed of 1 M $NaClO_4$ in a mixture of ethylene carbonate (EC) and diethyl carbonate (DEC) (1:1, in vol%). Lithium foil was employed as both counter and reference electrodes for LIBs. The electrolyte was composed of a solution of 1 M $LiPF_6$ in ethylene carbonate (EC)/dimethyl carbonate (DMC)/diethyl carbonate (DEC) (1:1:1, in vol%). A microporous membrane (Gelgard 2500) was used as the separator. The charge–discharge measurements were conducted using a multichannel battery testing system (LAND CT2001A) over a potential range from 0.01 to 3.00 V. Cycle voltammetry (CV) (0.01–3.00 V, 0.1 mv s^{-1}) and electrochemical impedance spectroscopy (EIS) (10 mHZ–1 MHZ) was using VSP-300 electrochemical workstation (Bio-logic, France). All electrochemical tests were carried out at room temperature.

3 Results and discussion

Figure 1 illustrates the synthesis route of the EWPC-T by a facile and effective way. Egg white was strongly stirred into foam and then water was removed by freeze-drying, while the color turned from yellow to white. The black powder was obtained after high temperature carbonization. Subsequently, the black powder was grinded by agate mortar and immersed in 80 °C deionized water. Finally, the sample was washed with deionized water and ethanol several times and dried at 80 °C in a vacuum oven overnight.

The thermal gravimetric (TG) curve (Fig. 2a) of the freeze-dried egg white obtained in a nitrogen atmosphere showed a plateau at temperature over 500 °C. Therefore, heating temperatures of 500, 600, 700 and 800 °C were chosen and the corresponding samples were denoted as EWPC-T (T = 500, 600, 700 and 800). Energy dispersive spectrometer (EDS) coordinating with scanning electron microscope (SEM) was used to analyze the composition and content of

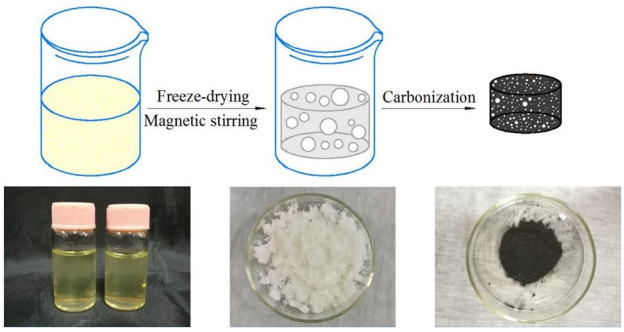

Fig. 1 Schematic illustration of synthesis of EWPC-T

the component elements in the material. The typical cheese structure was presented (Fig. 2b), cheese structure usually has multi-channel three-dimensional porous structure, which could shorten the transmission distance of ions and electrons, and improve the charge transfer efficiency. From Fig. 2c, carbon, nitrogen and oxygen element was uniformly distributed on the sample. Moreover, nitrogen element was successfully doped in the carbon material. Therefore, nitrogen doped carbon materials have been achieved by one-step carbonization without extra nitrogen source. Oxygen is commonly found in biomass-derived carbon materials, and it is beneficial to form stable solid electrolyte interface (SEI) film in the previous circles. Stable SEI film can maintain the structural integrity of electrode and prevent the failure of electrode structure. Oxygen and sulfur were mainly derived from proteins and fats in egg white. Unfortunately, no sulfur was found in the element maps, which is probably due to the low sulfur content (only 0.75%), demonstrated by the result of XPS tests (Fig. 5).

To investigate the influence of the carbonization temperature on the chemical composition of the sample, FTIR investigations was carried out. As shown in Fig. 3a, all samples presented similar FTIR spectra. A broad absorption band centered approximately at 3425 cm^{-1} is attributed to the O–H stretching vibrations. The strong absorption band centered at 1627 cm^{-1} is ascribed to C=C stretching vibrations. The relatively weak bands centered at 1390 cm^{-1} and 1500 cm^{-1} are attributed to C–C stretching vibrations and C–N bending vibration. The relatively broad band centered approximately at 1110 cm^{-1} could result from C–O stretching vibrations [16]. An obvious tend occurs that the intensity of C–O bond was gradually weakened with increasing the temperature. Figure 3b shows the XRD patterns of these samples. The broad bump centered at 24°, which is correspond to the [002] diffraction of carbon, indicating the amorphous nature and low graphitization degree.

Raman spectra of EWPC-T are shown in Fig. 3c–e. The Raman shifts located at 1352 cm^{-1} and 1583 cm^{-1} is related with the D and G bands (Fig. 3c), respectively. The intensity of the D band represents the disordered carbon and defects, while the G band indicates the degree of graphitized carbon. The intensity ratio of D to G bands (I_D/I_G) reflected the ratio

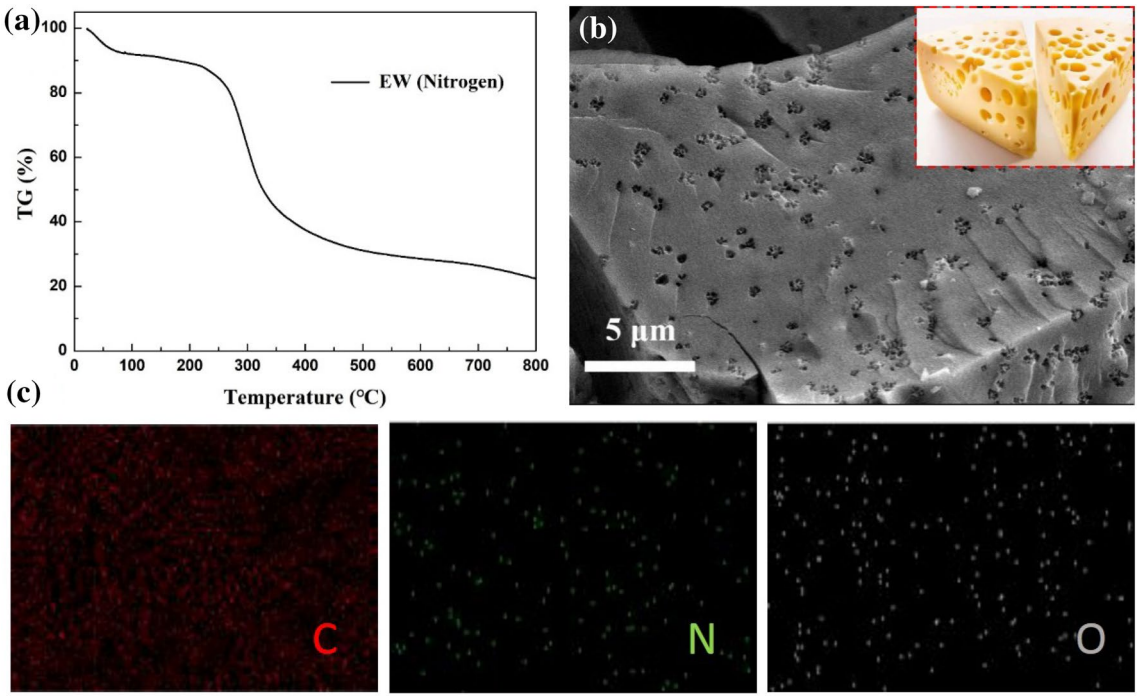

Fig. 2 **a** TGA curve of the freeze-dried egg white, **b**, **c** SEM image and element mappings of EWPC-T

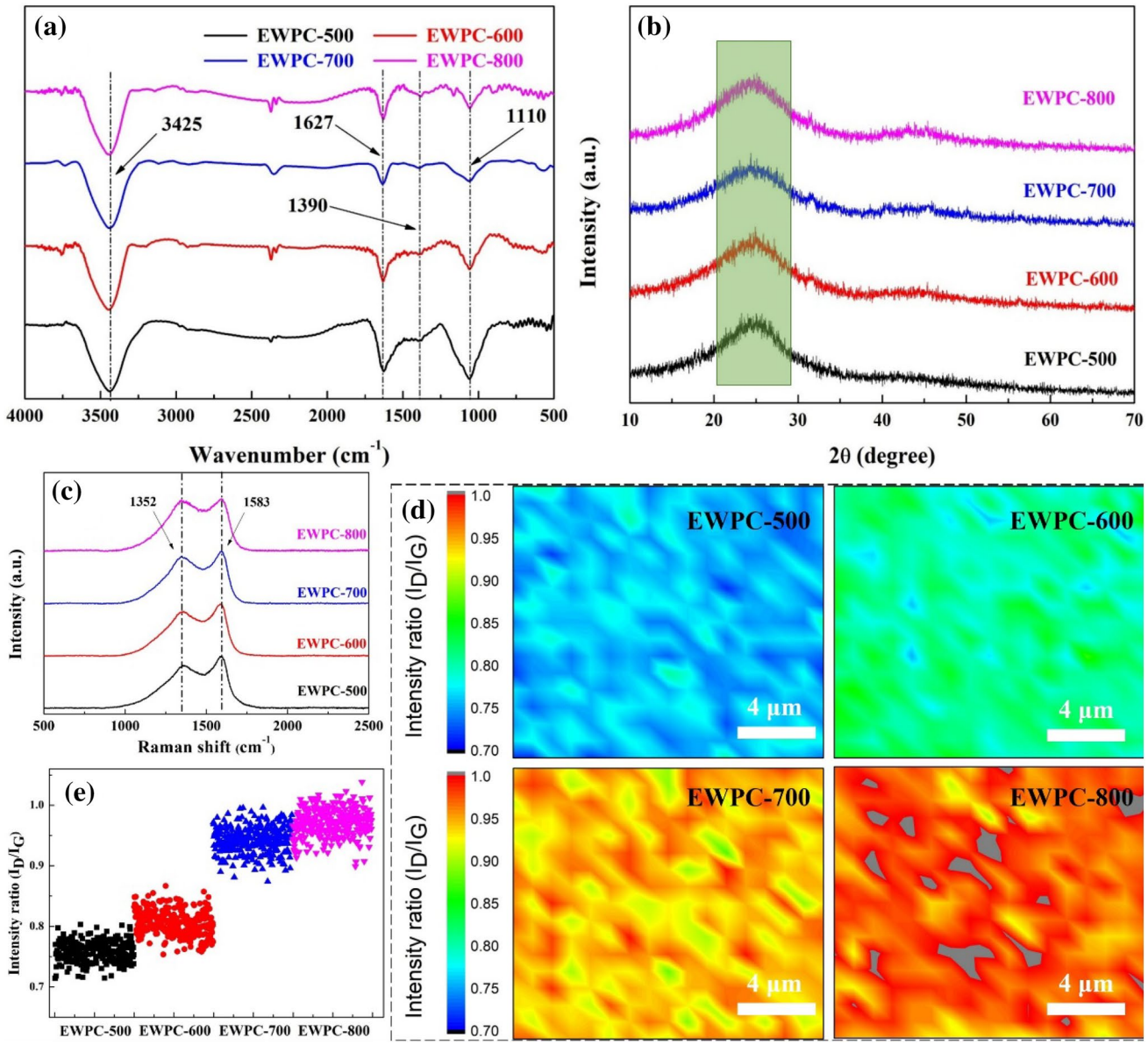

Fig. 3 **a** FTIR spectra and **b** XRD patterns of EWPC-T. **c** Raman spectra, **d** two dimensional Raman mappings and **e** the scatter plot made from different temperature (I_D/I_G) is the abbreviation for D to G band intensity ratio of EWPC-T

of disordered carbon and ordered graphitized carbon [24, 25]. From two dimensional Raman mappings (Fig. 3d), there appears an obvious trend that the color changed from light to deep with increasing the carbonization temperature. The color distribution of EWPC-600 is very uniform, indicating that the uniformity of carbonization is better than others. The average D/G intensity ratios of 289 points (Fig. 3e) from each carbonization temperature were 0.76 (EWPC-500), 0.81 (EWPC-600), 0.94 (EWPC-700) and 0.97 (EWPC-800), respectively. Higher temperatures lead to an increase of D/G ratio. The in-plane crystallite sizes (La) of EWPC were calculated by the following equation [26, 27]:

$$La\ (\mathrm{nm}) = \left(2.4 \times 10^{-10}\right)\lambda^4 \left(\frac{I_D}{I_G}\right)^{-1}$$

where λ is Raman laser wavelength (532 nm), I_D and I_G are the relative intensities of D and G bands, respectively. The calculated results of La were 25.3 nm (EWPC-500), 23.7 nm (EWPC-600), 20.5 nm (EWPC-700) and 19.8 nm (EWPC-800), respectively. The results suggest that the size of graphitic crystal shrinks with increasing temperature during the carbonization process, which could be attributed to the curve of graphite layers [28].

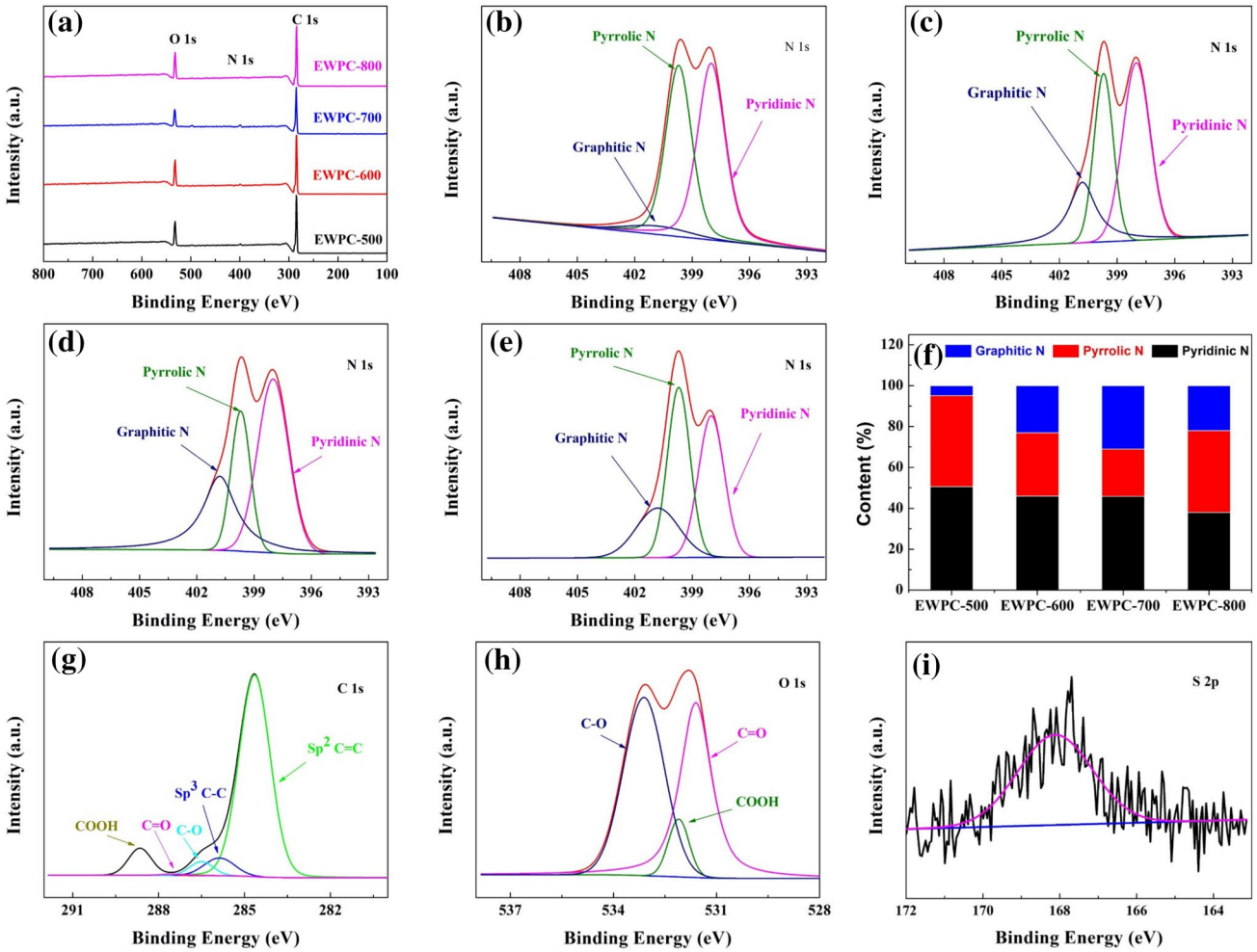

Fig. 4 **a** XPS survey spectra of EWPC-T. High-resolution N1s XPS spectrum of EWPC-500 (**b**), EWPC-600 (**c**), EWPC-700 (**d**) and EWPC-800 (**e**). **f** The contents of three types of nitrogen of EWPC-T. XPS narrow spectra of EWPC-600 of C1s (**g**), O1s (**h**) and S2p (**i**)

To further analyze the components of these samples, the corresponding XPS spectra of all samples are presented in Fig. 4. Figure 4a shows the XPS survey spectra. The contents of C1s, N1s and O1s are calculated to be EWPC-500 (68.1%, 4.1%, 27.3%), EWPC-600 (66.2%, 6.0%, 27.4%), EWPC-700 (67.7%, 3.7%, 28.3%) and EWPC-800 (69.1%, 2.8%, 28.1%). The high-resolution N1s XPS spectrum can be deconvoluted into three peaks (Fig. 4b–e), representing pyridinic N (N-6, 398.0 eV), pyrrolic N (N-5, 399.7 eV) and graphitic N (N-4, 400.8 eV) [29, 30]. According to the XPS statistical results (Fig. 4f), the EWPC-500 lacks graphitic N, which might result from the low carbonization temperature, leading to a decreased conductivity of carbon materials. EWPC-600 has higher pyridinic N and pyrrolic N than other samples. It is known that pyridinic N and pyrrolic N can create defects to provide active sites for sodium ion and lithium ion storage, while graphitic N can enhance the conductivity of carbon [29]. Figure 4g shows the high-resolution C1s spectrum of EWPC-600, which can be deconvoluted into five individual component peaks corresponding to $sp^2C{=}C$ (284.6 eV), $sp^3C{-}C$ (285.6 eV), C–O (286.5 eV), C=O (287.8 eV) and COOH (288.9 eV) [31–33]. The asymmetry trailing tails in C1s are caused by the inherent asymmetry of the graphite peaks or the contribution of the oxygen complexes on the surface. The O1s XPS core level spectrum (Fig. 4h) of EWPC-600 demonstrates the existence of three types of oxygen functionalities: C=O groups (531.7 eV), –COOH groups (532 eV) and C–O groups (533.2 eV). Among them, C=O groups are electrochemically active and the other two types of oxygen groups can improve the wettability of the carbon materials to electrolyte [23, 34]. What's more, eggs have a lot of protein, which usually contains a small amount of sulfur. Figure 4i shows the high-resolution S2p spectrum of EWPC-600, there occurred only one peak located at 166–170 eV, which stands for the different oxidized sulfur species ($C{-}SO_x{-}C$, $x = 2$–4) [35, 36]. Not only that, sulfur can easily disappear at high temperature and it cannot be observed for the samples prepared at 700

and 800 °C. As previously reported, it is believed that heteroatoms (for instance N, S and O) doping could offer high electronic conductivity and more advantaged active sites, which was favorable for enhancing reaction kinetics towards sodium and lithium ion storage.

Cheese-like biomass-derived carbon was used as electrode for sodium ion battery. Figure 5a shows the first and second charge–discharge profiles at 100 mA g^{-1}. During the first discharge (Na^+ insertion) process, each sample exhibited two small irreversible small platforms at around 0.7 V and 1.2 V, which were caused by solid-electrolyte interphase (SEI) formation or the side effect of sodium ion implantation. All samples present relatively low initial coulombic efficiency (ICE) of 31.92%, 41.28%, 42.83% and 48.8% for EWPC-500, EWPC-600, EWPC-700 and EWPC-800, respectively. At second cycle, no significant oxidation–reduction peak was observed and high coulombic efficiency was achieved. As shown in Fig. 5e, the cycling stability was tested at current density of 100 mA g^{-1}, EWPC-600 has highly reversible capacity (226.8 mA h g^{-1}), After 100 cycles, the specific capacity of EWPC-600 electrode reached 210.5 mA h g^{-1}, far higher than 86.6 (EWPC-500), 162.1 (EWPC-700) and 126.4 mA h g^{-1} (EWPC-800). EWPC-600 capacity retention rate is 92.8% and also has a high coulombic efficiency of ~ 100%, indicating that sodium ion insertion/extraction is highly reversible and displays outstanding cycling stability. The excellent sodium ion storage performance of EWPC-600 is attributed to high content of N

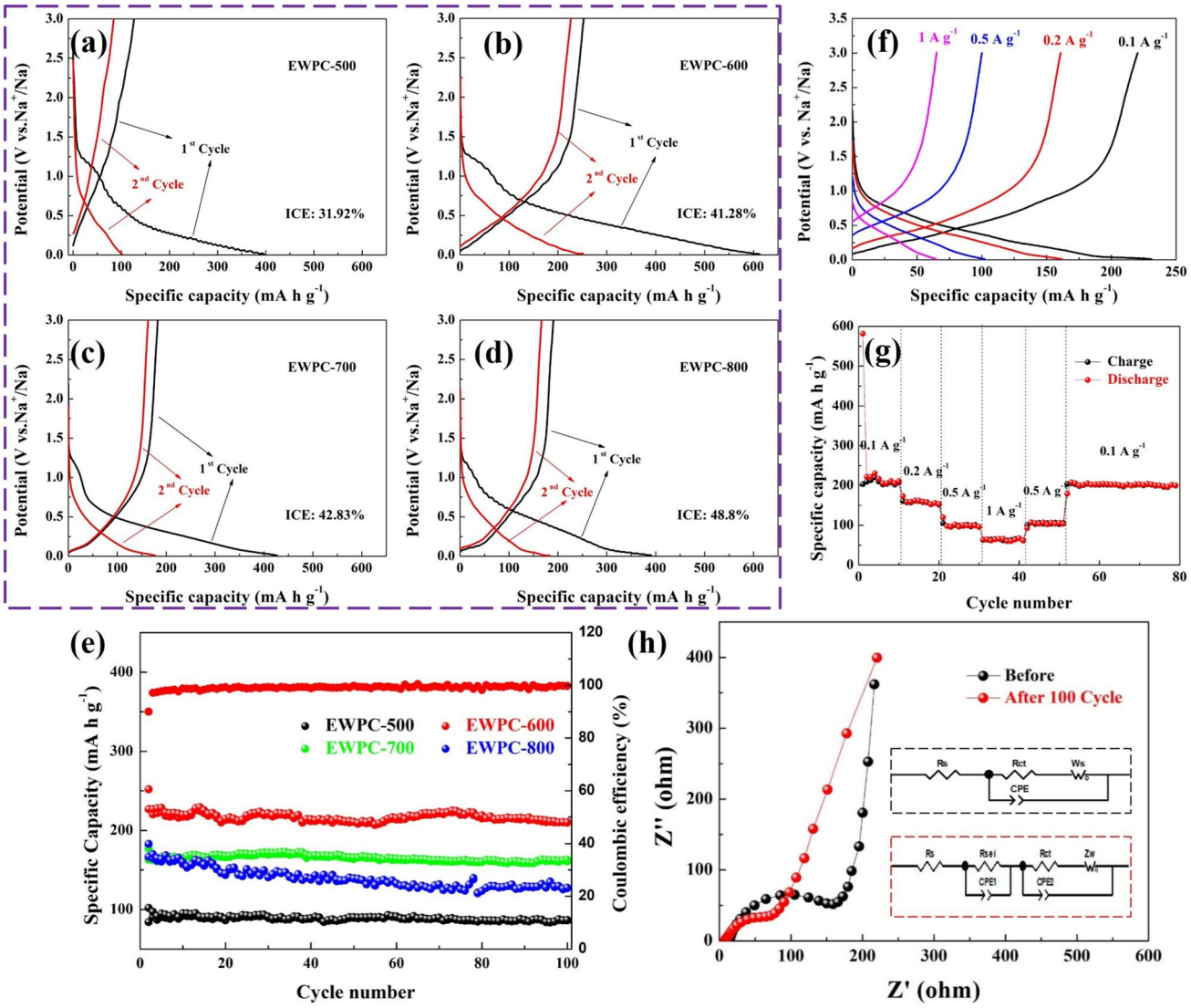

Fig. 5 Electrochemical characterization of EWPC-T for anode of SIBs: **a–d** the first and second charge–discharge profiles of EWPC-T; **e** cycling stability and the corresponding coulombic efficiency of EWPC-T at 100 mA g^{-1}; **f** The charge–discharge profiles of EWPC-600 at different current densities; **g** rate capabilities of EWPC-600 from 0.1 to 1 A g^{-1}; **h** Nyquist plots of EWPC-600 electrode before and after 100 cycles in the frequency range from 10 mHz to 1 MHz

element and trace amounts of S element co-doped, enhanced sodium ion adsorption and storage.

Figure 5f shows the charge and discharge profiles at 0.1, 0.2, 0.5 and 1 A g^{-1}, representing similar charge and discharge platform, which indicated that it can exhibit fine insertion and extraction under high current density. EWPC-600 also exhibits excellent rate ability, which is shown in Fig. 5g. After high current density charge–discharge process, EWPC-600 still maintains a high stable capacity when current density decreases back to 100 mA g^{-1}. Electrochemical impedance spectroscopy (EIS) experiments were further employed in the electrode reaction in the frequency range from 10 mHz to 1 MHz. Nyquist plots of EWPC-600 electrode before and after 100 cycles are shown in Fig. 5h. In the high frequency region, R_S is the internal resistance of tested battery (include electrolyte and cell component), R_{SEI} is related to the solid electrolyte interface (SEI) film on the carbon matrix, R_{ct} represents the charge transfer resistance through the electrode/electrolyte interface, CPE_1 and CPE_2 are associated with the constant phase element. The inclined line in the low frequency region corresponds to the Warburg impedance (Z_W) during the diffusion of the sodium into the bulk of electrode material [1]. Apparently, the diameter of high frequency semicircle gradually decreases after cycling, indicating that the electrodes have smaller charge transfer resistance, which may be due to the activation of electrode materials. All samples featured a typical quasi-vertical line at low frequencies and showed a narrower Warburg impedance region, suggesting that cheese-like biomass-derived carbon exhibits excellent ion diffusion behavior. Furthermore, EWPC-600 delivers a better capacity compared to other biomass-derived carbon materials (Table 1).

The electrochemical properties of cheese-like biomass-derived carbon material were also investigated as anodes of lithium ion batteries (LIBs). Figure 6a shows the CV curves of the initial five cycles. In the first discharge scan, there is a cathodic peak presented over a wide region attributed to complex phase transitions caused by Li intercalation into porous carbon. A broad peak at 0.5 V was observed, which could be attributed to the formation of solid electrolyte interface (SEI) film, and disappeared in the next cycles. As well as the other unknown irreversible reaction, the incomplete extraction of Li ion is the result of the lithium trap in porous electrodes partial release back in the first cycle, which is the main reason for the initial irreversible capacity. During the Li ion extraction process, wide peaks from 0.2 to 1.25 V can be found and are attributed to Li extraction from carbon layers and pores or defects. From the second cycle, the CV profiles show little difference with increasing the cycle, suggesting the loss of some irreversible lithium storage sites in EWPC-600 during the first cycle and a trend of getting stable in the latter cycles. Figure 6b displays the charge–discharge curves of the EWPC-600 electrode at 100 mA g^{-1}. It is evident that the plateaus are consistent with the respective peaks of the above CV results. The sloped discharge plateau lower than 0.5 V is due to interfacial Li ion uptake by carbon material. The EWPC-600 electrode exhibits an initial discharge capacity of 1639.4 mA h g^{-1} and charge capacity of 872.6 mA h g^{-1} with a coulombic efficiency of 53.23%. The decreased large irreversible lithium storage in the first cycle is due to a large number of side reactions occurring during the first lithium insertion process.

As shows in Fig. 6c, the cycle stability of each sample was tested by using GCD process at current density of 100 mA g^{-1}. After eighty cycles, the specific capacity of EWPC-600 electrode reached 567.5 mA h g^{-1}, far higher than EWPC-500 (278.8 mA h g^{-1}), EWPC-700 (268.6 mA h g^{-1}) and EWPC-800 (311.9 mA h g^{-1}). As shows in Fig. 6d, the cycle stability of each sample was tested at a current density of 1000 mA g^{-1}. Compared to the other samples, EWPC-600 delivered the highest specific capacity and excellent cyclical stability, which also caused by the high content of N element and trace amounts of S element co-doping of EWPC-600. EWPC-600 also represents excellent rate ability, shown in Fig. 6e. Figure 6f exhibits long-term cycling performance of the EWPC-600 electrode at a current density of 1.0 A g^{-1}. It delivers discharge capacity of 286.8 mA h g^{-1} in the second cycle, which increases to 300.6 mA h g^{-1} in the following 800 cycles (capacity retention ratio is 104.8%). It is indicated that the prepared cheese-like biomass-derived carbon exhibits excellent electrochemical performance. In addition, the performance of EWPC-600 is superior to most of other biomass-derived carbon materials as the anode of LIBs as shown in Table 2.

Table 1 Comparison of the results in this work with partially reported electrochemical properties of biomass derived carbon materials for SIBs anodes

Carbon source	Current density (mA g^{-1})	Specific capacity (mA h g^{-1})	References
Pomelo peels	200	181	[37]
Lignin	50	297	[4]
Rice husk	100	170	[3]
Loofah sponge	100	100	[38]
Algae-carragen	100	227	[23]
Citrus peel	100	140	[39]
Peanut shell	250	193	[18]
Sucrose	100	220	[40]
Egg white	100	226.8	This work

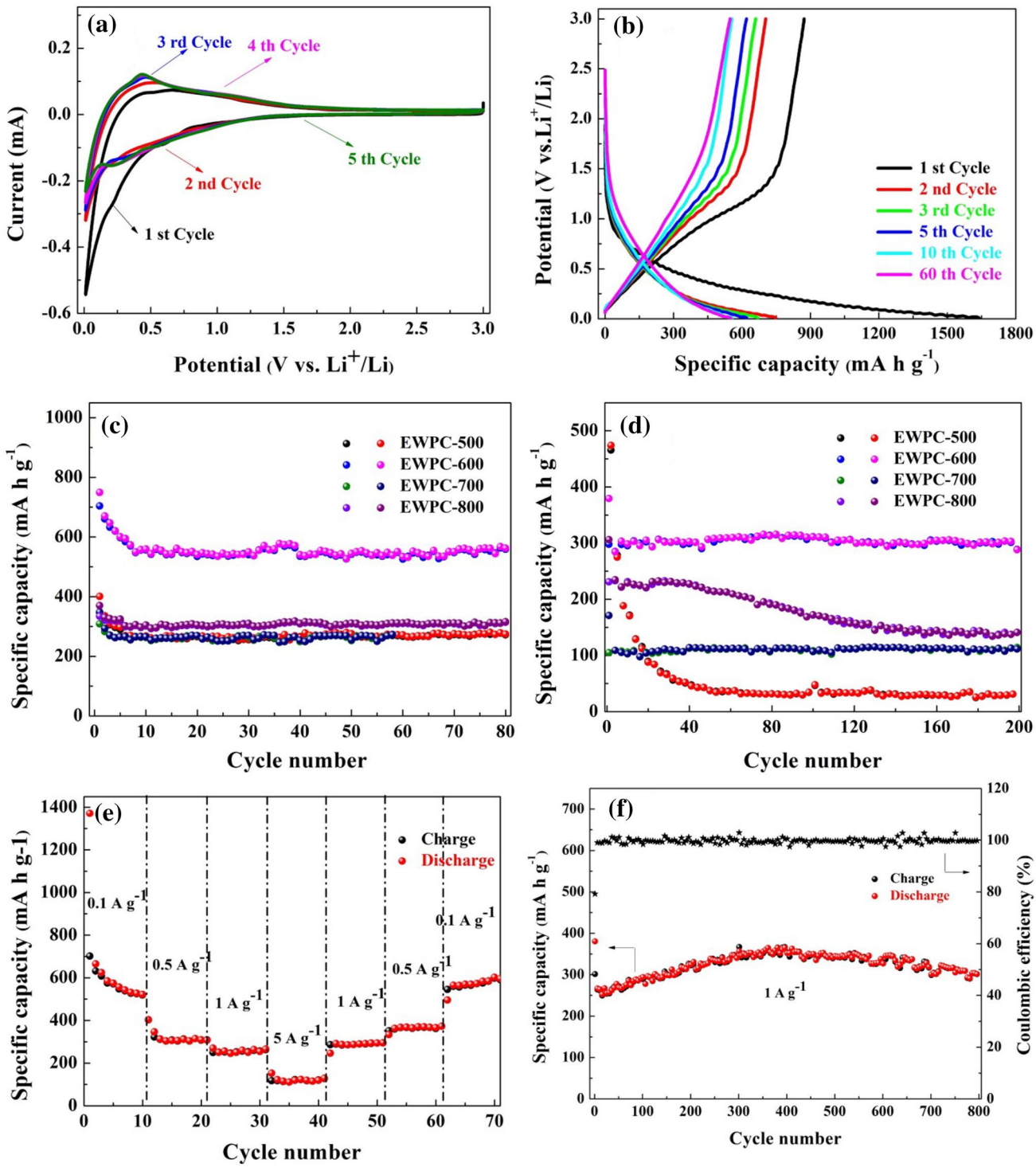

Fig. 6 Electrochemical characterization of EWPC-T for anode of LIBs: **a** CV curves of EWPC-600 at a scan rate of 0.1 mv s^{-1}; **b** the charge–discharge profiles of EWPC-600 at 100 mA g^{-1}; cycle stability of EWPC-T at **c** 100 mA g^{-1} and **d** 1000 mA g^{-1}; **e** rate capabilities of EWPC-600 from 0.1 to 5 A g^{-1}; **f** long-term cycling performance and coulombic efficiency of EWPC-600 at 1.0 A g^{-1}

4 Conclusions

In summary, a facile and effective approach was developed to transform the egg white into cheese-like biomass-derived carbon electrodes with plentiful heteroatoms for sodium-ion batteries (SIBs) and lithium-ion batteries (LIBs). Cheese-like structure and plentiful heteroatoms not only provide a short-circuit ion–electron transport channel, but also

Table 2 Comparison of the results in this work with partially reported electrochemical properties of biomass derived carbon materials for LIBs anodes

Carbon source	Current density (mA g^{-1})	Specific capacity (mA h g^{-1})	References
Corn starch	100	507	[41]
Pollen	C/10	382	[42]
Kiwifruit	100	504.8	[16]
Bean dreg	100	423	[31]
Banboo	171	353	[21]
Human hair	300	350	[43]
Peanut shell	1000	474	[18]
Egg white	100	567.5	This work

improve the conductivity and add a large number of active sites. Beneficial from the reasonable arrangement, the as-prepared electrode exhibits significantly enhanced sodium storage properties including highly reversible capacity (226.8 mA h g^{-1} at 100 mA g^{-1}), superior rate capability and excellent capacity retention (92.8%), great lithium ion capacity (567.5 mA h g^{-1} after 80 cycles at 100 mA g^{-1}), fine rate capability and outstanding capacity retention (104.8%). This work could provide a facile and effective way to translate biomass into useful carbon materials for applications not only in SIBs and LIBs, but also in other type energy storage, such as lithium–sulfur batteries, supercapacitors, etc.

Acknowledgements We greatly acknowledge the funding for this project through the National Natural Science Foundations of China (No. 51873083), the Opening Project of State Key Laboratory of Polymer Materials Engineering (Sichuan University) (No. sklpme2018-4-27), the Six Talent Peaks Project in Jiangsu Province (No. 2015-XCL-028) and the Postgraduate Research and Practice Innovation Program of Jiangsu Province (KYCX17_1831, SJCX18_0759).

Compliance with ethical standards

Conflict of interest The authors declare that they have no conflicts to declare.

References

1. N. Mahmood, T. Tang, Y. Hou, Adv. Energy Mater. **6**, 1600374 (2016). https://doi.org/10.1002/aenm.201600374
2. X.-C. Zhao, P. Yang, L.-J. Yang et al. ES Mater. Manuf. (2018). https://doi.org/10.30919/esmm5f109
3. Q. Wang, X. Zhu, Y. Liu, Y. Fang, X. Zhou, J. Bao, Carbon **127**, 658 (2018). https://doi.org/10.1016/j.carbon.2017.11.054
4. D. Yoon, J. Hwang, W. Chang, J. Kim, ACS Appl. Mater. Interfaces **10**, 569 (2018). https://doi.org/10.1021/acsami.7b14776
5. X. Liu, D. Chao, Y. Li et al., Nano Energy **17**, 43 (2015). https://doi.org/10.1016/j.nanoen.2015.07.029
6. W. Liu, Z. Chen, G. Zhou et al., Adv. Mater. **28**, 3578 (2016). https://doi.org/10.1002/adma.201505299
7. H. Zhang, G. Cao, Y. Yang, Energy Environ. Sci. **2**, 932 (2009). https://doi.org/10.1039/b906812k
8. L. Qie, W.M. Chen, Z.H. Wang et al. Adv. Mater. **24**, 2047. (2012). https://doi.org/10.1002/adma.201104634
9. A.D. Roberts, X. Li, H. Zhang, Chem. Soc. Rev. **43**, 4341 (2014). https://doi.org/10.1039/c4cs00071d
10. S. Arunachalam, B. Kirubasankar, V. Murugadoss, D. Vellasamy, S. Angaiah, New J. Chem. **42**, 2923 (2018). https://doi.org/10.1039/C7NJ04335J
11. A. Subasri, K. Balakrishnan, E.R. Nagarajan, V. Devadoss, A. Subramania, Electrochim. Acta **281**, 329 (2018). https://doi.org/10.1016/j.electacta.2018.05.142
12. Q. Du, Y. Zhou, X. Pan et al., RSC Adv. **6**, 54589 (2016). https://doi.org/10.1039/C6RA08412E
13. J. Wang, P. Nie, B. Ding et al., J. Mater. Chem. A **5**, 2411 (2017). https://doi.org/10.1039/c6ta08742f
14. Z. Qu, M. Shi, H. Wu, Y. Liu, J. Jiang, C. Yan, J. Power Sources **410–411**, 179 (2019). https://doi.org/10.1016/j.jpowsour.2018.11.018
15. X. Wang, X. Zeng, D. Cao, Eng. Sci. (2018). https://doi.org/10.30919/es.180325
16. C. Wang, Y. Xiong, H. Wang, C. Jin, Q. Sun, J. Mater. Chem. A **5**, 15759 (2017). https://doi.org/10.1039/c7ta04178k
17. H. Yin, B. Lu, Y. Xu et al., Environ. Sci. Technol. **48**, 8101 (2014). https://doi.org/10.1021/es501739v
18. W. Lv, F. Wen, J. Xiang et al., Electrochim. Acta **176**, 533 (2015). https://doi.org/10.1016/j.electacta.2015.07.059
19. Z. Sun, S. Wang, L. Yan, M. Xiao, D. Han, Y. Meng, J. Power Sources **324**, 547 (2016). https://doi.org/10.1016/j.jpowsour.2016.05.122
20. B. Li, Z. Xiao, M. Chen et al., J. Mater. Chem. A **5**, 24502 (2017). https://doi.org/10.1039/c7ta07088h
21. J. Jiang, J. Zhu, W. Ai et al., Energy Environ. Sci. **7**, 2670 (2014). https://doi.org/10.1039/c4ee00602j
22. Y. Cheng, S. Ji, X. Xu, J. Liu, RSC Adv. **5**, 100089 (2015). https://doi.org/10.1039/c5ra21416e
23. M. Lu, W. Yu, J. Shi et al., Electrochim. Acta **251**, 396 (2017). https://doi.org/10.1016/j.electacta.2017.08.131
24. A.C. Ferrari, Solid State Commun. **143**, 47 (2007). https://doi.org/10.1016/j.ssc.2007.03.052
25. B. Kirubasankar, V. Murugadoss, J. Lin et al., Nanoscale **10**, 20414 (2018). https://doi.org/10.1039/C8NR06345A
26. F. Banhart, J. Kotakoski, A.V. Krasheninnikov, ACS Nano **5**, 26 (2011). https://doi.org/10.1021/nn102598m
27. D.G. Lim, K. Kim, M. Razdan, R. Diaz, S. Osswald, V.G. Pol, Carbon **121**, 134 (2017). https://doi.org/10.1016/j.carbon.2017.05.079
28. L.G. Cançado, K. Takai, T. Enoki et al., Appl. Phys. Lett. **88**, 163106 (2006). https://doi.org/10.1063/1.2196057
29. C. Wang, D. Wu, H. Wang, Z. Gao, F. Xu, K. Jiang, J. Mater. Chem. A **6**, 1244 (2018). https://doi.org/10.1039/c7ta07579k
30. X. Pan, Q. Du, Y. Zhou, L. Liu, G. Xu, C. Yan, J. Nanosci. Nanotechnol. **18**, 7231 (2018)
31. H. Ru, K. Xiang, W. Zhou, Y. Zhu, X.S. Zhao, H. Chen, Electrochim. Acta **222**, 551 (2016). https://doi.org/10.1016/j.electacta.2016.10.202
32. Q. Zhang, K. Han, S. Li, M. Li, J. Li, K. Ren, Nanoscale **10**, 2427 (2018). https://doi.org/10.1039/c7nr07158b
33. L. Wang, H. Zhang, W. Zhang et al., Chem. Eng. J. **337**, 201 (2018). https://doi.org/10.1016/j.cej.2017.12.089
34. X. Dong, H. Jin, R. Wang et al., Adv. Energy Mater. (2018). https://doi.org/10.1002/aenm.201702695
35. Y. Yan, Y.-X. Yin, S. Xin, Y.-G. Guo, L.-J. Wan, Chem. Commun. **48**, 10663 (2012). https://doi.org/10.1039/C2CC36234A
36. L. Miao, D. Zhu, M. Liu et al., Electrochim. Acta **274**, 378 (2018). https://doi.org/10.1016/j.electacta.2018.04.100

37. K. Hong, L. Qie, R. Zeng et al., J. Mater. Chem. A **2**, 12733 (2014). https://doi.org/10.1039/c4ta02068e
38. D. Xie, X. Xia, W. Tang et al., J. Mater. Chem. A **5**, 7578 (2017). https://doi.org/10.1039/c7ta01154g
39. N.R. Kim, Y.S. Yun, M.Y. Song et al., ACS Appl. Mater. Interfaces **8**, 3175 (2016). https://doi.org/10.1021/acsami.5b10657
40. L. Xiao, H. Lu, Y. Fang et al., Adv. Energy Mater. (2018). https://doi.org/10.1002/aenm.201703238
41. M. Chen, C. Yu, S. Liu et al., Nanoscale **7**, 1791 (2015). https://doi.org/10.1039/c4nr05878j
42. J. Tang, V.G. Pol, Sci. Rep. **6**, 20290 (2016). https://doi.org/10.1038/srep20290
43. K.R. Saravanan, N. Kalaiselvi, Carbon **81**, 43 (2015). https://doi.org/10.1016/j.carbon.2014.09.021